# Neutral outflows in high-redshift dusty galaxies

Butler, K.M.

# 4 | Neutral Outflows in High–z QSOs

Adapted from

K. M. Butler, P. P. van der Werf, A. Omont, P. Cox

*Astronomy & Astrophysics, in press*

$OH^+$ absorption has proven to be a powerful tracer of inflowing and outflowing gas in the predominantly atomic diffuse turbulent halo surrounding galaxies. In this letter, we present observations of $OH^+(1_1\text{-}1_0)$, CO(9-8) and the underlying dust continuum in five $z \sim 2-4$ QSOs using the Atacama Large Millimeter/submillimeter Array (ALMA) with the aim of detecting outflowing neutral gas. Blue-shifted $OH^+(1_1\text{-}1_0)$ absorption is detected in 3/5 QSOs, tentatively in a fourth and at the systemic velocity in one source. $OH^+(1_1\text{-}1_0)$ emission is observed in 3/5 QSOs at systemic velocities and the $OH^+(2_1\text{-}1_0)$ transition is also detected in one source. CO(9-8) is detected in all 5 QSOs at high S/N, providing information on the dense molecular gas within the host galaxy. We compare our sample to far-infrared (FIR) luminous high-$z$ star–forming and active galaxies from the literature. We find no difference in $OH^+$ absorption line properties between active and star–forming galaxies with both samples roughly following the same optical depth – dust temperature relation, suggesting that these observables are driven by the same mechanism in both samples. $OH^+$ emission line luminosity similarly follows the same relation with FIR luminosity between star–forming and active galaxies. Obscured QSOs, however, display broader ($> 800\,\mathrm{km\,s^{-1}}$) emission than the unobscured QSOs and all but one star–forming galaxies, possibly indicating a higher contribution from X-ray dominated regions in obscuring material close to the accreting nucleus. The obscured QSOs seem to display broader CO(9-8) emission ($> 500\,\mathrm{km\,s^{-1}}$) than the unobscured QSOs, but cover a similar range in line widths as the star-forming galaxies. The QSO sample follows the CO(9-8)–FIR luminosity relation found in low–$z$ galaxies. We find that outflows traced by $OH^+$ are only detected in extreme (indicated by broad CO(9-8) emission) star–forming galaxies, but in both types of QSOs, which in turn display no red–shifted absorption. This suggests that diffuse neutral outflows in the halo may be associated with the most energetic evolutionary phase leading up to the obscured QSO phase and into the unobscured phase.



## 4.1 Introduction

Feedback and outflows play a key role in the evolution, regulation and ultimate demise of galaxies throughout cosmic time. Much of the gas accreted onto dark matter halos, and consequently their central galaxies where it condenses to form new stars or feed supermassive black hole growth, is ejected back out of the galaxy via the energetic mechanisms associated with these phenomena. The removal of gas regulates the fuel available for galaxy growth, transporting mass and angular momentum to higher galactic radii (Governato et al., 2010) via fountain flows or, in more powerful cases, into the circum– and inter–galactic medium polluting it with enriched gas (Travascio et al., 2020). At $z \sim 1-3$ the star formation rate density and black hole accretion

peaks in the universe (Madau & Dickinson, 2014), and thus so must feedback and outflows.

Outflows are complex multi–phase phenomena, in which the warmer ionised phase is found to dominate the kinetic energy, whilst the cooler neutral and molecular phases dominate the mass and momentum budget of the outflow (Fluetsch et al., 2021). The cooler phases are of particular interest as they remove the direct fuel for star formation, but have only become available for observation at high–$z$ relatively recently with new and upgraded facilities such as ALMA and the NOrthern Extended Millimeter Array (NOEMA).

Low–$z$ studies have commonly made use of high velocity line wings of bright emission lines such as CO to detect outflows (Feruglio et al., 2010), however at high–$z$ detecting these weak signals from CO or [CII] become difficult (e.g., Fan et al., 2018; Ginolfi et al., 2020). Blue-shifted molecular absorption lines have thus become a popular and reliable way of detecting and studying cool gas outflows both at cosmic noon (e.g., $OH^+$ :Butler et al. 2021; Riechers et al. 2021; Shao et al. 2022; $CH^+$ : Falgarone et al. 2017) and dawn (e.g., OH 119 $\mu m$: Spilker et al. 2018, 2020; Butler et al. 2023; $H_2O$: Jones et al. 2019).

Of note in this selection is $OH^+$, which traces the extended turbulent halo of predominantly atomic and diffuse gas surrounding galaxies (Indriolo et al., 2018).Moreover, the proximity of the $OH^+(1_1\text{-}1_0)$ transition to the CO(9-8) emission line means that simultaneous observations of warm molecular gas can be made, providing additional information on the physical properties within the galaxy (Berta et al., 2021; Riechers et al., 2021). Currently, however, observations are limited to star-forming galaxies (Butler et al. 2021; Riechers et al. 2021; Berta et al. 2021; Indriolo et al. 2018; Shao et al. 2022, Butler et al. in prep.), with only a few observations in active galaxies (Stanley et al., 2021; Shao et al., 2019, 2022).



In this letter, we present $OH^+(1_1\text{-}1_0)$, CO(9-8) and dust continuum observations in five $z$∼2−4 far-infrared (FIR) bright QSOs. Throughout this work we adopt a flat ΛCDM cosmology with $\Omega_m = 0.307$ and $H_0 = 67.7$ km s$^{-1}$ Mpc$^{-1}$ (Planck Collaboration et al., 2016).

## 4.2 Sample and Observations

The data were obtained in the Cycle 7 ALMA project 2019.1.01802.S (P.I.: K.M. Butler) targeting 5 FIR–bright QSOs at $z \sim 2-4$: HE 1104−1805, MG J0414+0534, PSS J2322+1944, RX J0911+0551 and WFI J2026−4536. The five quasars were selected based on their 500 $\mu$m continuum flux densities

from a sample of 104 gravitationally lensed QSOs presented in Stacey et al. (2018). The sources are listed in both the CASTLES survey (Kochanek et al., 1999) and Sloan Digital Sky Survey Quasar Lens Search catalogue (Inada et al., 2012), and have since been followed up with *Herschel*/SPIRE observations (Stacey et al., 2018), providing accurate estimates of their FIR-luminosities and dust temperatures (Table 4.3). The selected sample covers ∼ 2 decades in dust temperature, ∼ 1 order of magnitude in $L_{FIR}$ and includes one quasar with a jet-dominated radio emission, MG J01414+0534 (Stacey et al., 2018).

All sources were observed with ALMA band 7, except PSS J2322+1944 which was observed in band 5. The receivers were tuned such that two overlapping spectral windows cover the $OH^+(1_1\text{-}1_0)$ and CO(9-8) lines in one sideband, and the two remaining spectral windows were placed to detect the underlying dust continuum at high signal to noise in the other sideband (Fig. 4.1). No calibration issues were found, and observations were all made during good or

adequate weather conditions.

The raw data were reduced using CASA (McMullin et al., 2007). The calibrated data were non-interactively imaged using a robust weighting of 0.5 and noise threshold of $1\sigma$ with the `tclean` routine. We do not subtract the continuum, and separate the sidebands into two cubes, leaving the frequency resolution at that of the receiver channels (15.624 MHz).

## 4.3 Spectra and Spectral Fitting

We present both sidebands of the ALMA spectra for each source in Fig. 4.1. The spectra are created and fitted twice: first by summing over all spaxels with a S/N $\geq 3\sigma$ in the underlying dust continuum and secondly by also summing over all spaxels containing a channel value $\geq 3\sigma$ within the FWHM of one or more of the CO(9-8) components found in the first fitting procedure. We fit all spectral line components and a linear continuum slope simultaneously, leaving the central frequencies, line widths, intensities and continuum gradient as free parameters. We use the same line parameters to describe the $OH^+(1_1\text{-}1_0)$ and $OH^+(2_1\text{-}1_0)$ transitions detected in PSS J2322+1944 and RX J0911+0551. We provide updated redshifts for HE 1104−1805 of $z = 2.3222 \pm 0.0001$, centered on the $OH^+(1_1\text{-}1_0)$ emission line, and WFI J2026−4536 $z = 2.24265 \pm 0.00001$, centered in the CO(9-8) line (Table 4.3). The best–fit parameters of the second integration and fit are presented in Tables 4.1 and 4.2.

## 4.4 Results

We present the main line properties derived from the fitted $OH^+$ absorption, emission and CO(9-8) emission in our sample of high-$z$ quasars. These properties are then compared to results obtained on high-$z$ quasars and dusty star-forming galaxies (DSFGs) galaxies with comparable FIR luminosities including the Hot Dust Obscured Galaxy (Hot DOG) W0410−0913 ($z$=3.592, Stanley et al. 2021), the unobscured QSO SDSS J231038.88+185519.7 ($z$=6.0031, Shao et al. 2022), high-$z$ DSFGs from Riechers et al. (2021) and the Herschel/H-ATLAS DSFG HerBS-89a ($z$=2.95, Berta et al. 2021).

### 4.4.1 Fitted Line Properties

Blue-shifted $OH^+$ absorption is detected in 3/5 QSOs, with one source, the only obscured and jetted QSO, MG J0414+0534, also displaying weak absorption at the systemic velocity (Fig. 4.1, Table 4.1). We include RX J0911+0551 as a tentative detection as it appears in both the $OH^+(1_1\text{-}1_0)$ and $OH^+(2_1\text{-}1_0)$ transitions but stress that these values are uncertain. No red–shifted absorption was found, unlike some of the sources reported in Riechers et al. (2021) or the case of HerBS-89a described in Berta et al. (2021). Blue–shifted velocities and linewidths are not boosted with respect to the DSFGs. The QSOs do, however, show a trend between faster outflow velocity and wider outflow full width half maximum (FWHM); however, a larger sample is needed to confirm this trend.

$OH^+$ emission is found in 3/5 QSOs, all at systemic velocities unlike the DSFGs presented in Riechers et al. (2021), which display a large spread in velocity offsets between the $OH^+$ and

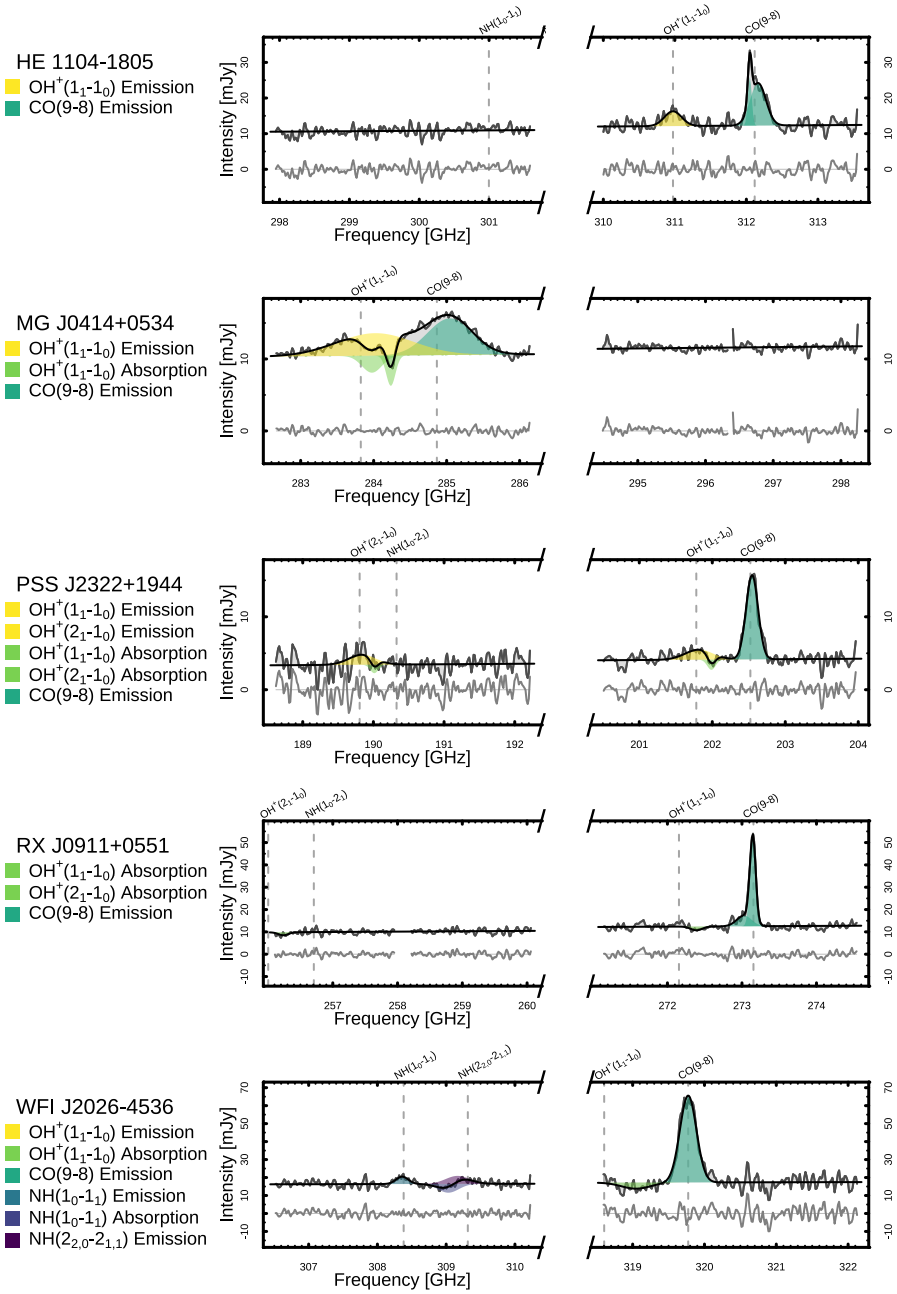


Figure 4.1: *Spatially integrated spectra, fits and residuals of the 5 QSOs. Observed frequencies are displayed on the horizontal axis and the expected redshifted rest frequencies of the spectral lines are indicated by vertical dashed lines.*

Table 4.1: Observed properties of the dust continuum and the $OH^+(1_1 - 1_0)$

| Name | $Cont_{1033.119}$* | $OH^+(1_1 - 1_0)$ Absorption | | | $OH^+(1_1 - 1_0)$ Emission | | |
|---|---|---|---|---|---|---|---|
| | S | S | v | $\sigma$ | S | v | $\sigma$ |
| | [mJy] | [Jy km s$^{-1}$] | [km s$^{-1}$] | [km s$^{-1}$] | [Jy km s$^{-1}$] | [km s$^{-1}$] | [km s$^{-1}$] |
| MG J0414+0534 | 10.4 ± 2.4 | −0.73 ± 0.17 | −162 ± 16 | 144 ± 22 | 4.33 ± 0.38 | −207 ± 49 | 552 ± 54 |
| | | −0.60 ± 0.07 | −435 ± 4.9 | 67.0 ± 5.2 | | | |
| RX J0911+0551 | 15.9 ± 0.74 | −0.28 ± 0.06 | −253 ± 21 | 84.6 ± 21 | | | |
| HE 1104-1805 | 12.1 ± 1.1 | | | | 1.20 ± 0.15 | 199 ± 15 | 116 ± 16 |
| WFI J2026-4536 | 7.78 ± 2.6 | −1.49 ± 0.34 | −357 ± 41 | 190 ± 34 | | | |
| PSS J2322+1944 | 5.79 ± 0.77 | −0.25 ± 0.13 | −308 ± 25 | 84.8 ± 32 | 0.98 ± 0.22 | −56.0 ± 71 | 284 ± 48 |

**Note:** *: Continuum flux at 1033.119 GHz rest frequency (i.e. the $OH^+(1_1 - 1_0)$ transition rest frame frequency). Uncertainties are taken from those given by the fitting procedure in `curve_fit` and may underestimate the $OH^+$ flux errors in the case of MG J0414+0534 and PSS J2322+1944 where the line has been broken up into multiple components. Consequently, the deblending of the broad $OH^+$ and CO(9-8) emission lines in MG J0414+0534 may not be unique. See Fig. 4.1 for observed frequencies.

Table 4.2: Observed properties of the CO(9-8) lines.

| Name | CO(9 − 8) Emission | | |
|---|---|---|---|
| | S | v | $\sigma$ |
| | [Jy km s$^{-1}$] | [km s$^{-1}$] | [km s$^{-1}$] |
| MG J0414+0534 | 4.12 ± 0.28 | −186 ± 15 | 324 ± 12 |
| RX J0911+0551 | 4.14 ± 0.36 | 15.5 ± 1.2 | 42.6 ± 0.37 |
| | 1.32 ± 0.45 | 142 ± 42 | 110 ± 25 |
| HE 1104-1805 | 0.89 ± 0.13 | 264 ± 3.0 | 26.2 ± 3.0 |
| | 3.16 ± 0.22 | 154 ± 6.5 | 106 ± 6.5 |
| WFI J2026-4536 | 13.1 ± 0.31 | 60.3 ± 2.6 | 108 ± 2.8 |
| PSS J2322+1944 | 3.54 ± 0.093 | −34.7 ± 3.4 | 122 ± 3.5 |

**Note:** Uncertainties are taken from those given by the fitting procedure in `curve_fit`. See Fig. 4.1 for observed frequencies.



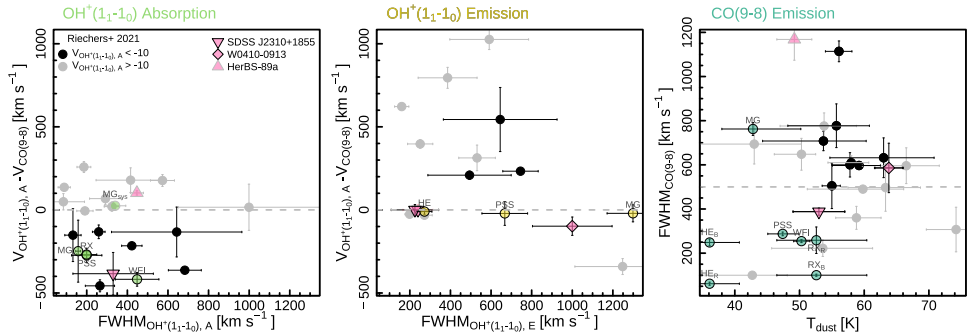


Figure 4.2: *Comparing line properties of* $OH^+$ *and CO(9-8) between the QSO sample of this work with other high–z QSOs (Stanley et al., 2021; Shao et al., 2022) and DSFGs (Berta et al., 2021; Riechers et al., 2021) from the literature. In all panels, we colour the sources from Riechers et al. (2021) with blue–shifted* $OH^+$ *absorption in black and colour the rest of the sample in grey.* ***Left:*** $OH^+$ *absorption FWHM vs velocity w.r.t. the CO(9-8) emission.* ***Middle:*** $OH^+$ *emission FWHM vs velocity w.r.t. the CO(9-8) emission.* ***Right:*** *Dust temperature vs CO(9-8) emission FWHM (of the broadest CO component in each source). FWHMs are derived by multiplying the velocity dispersions in Table 4.2 by a factor of* $2\sqrt{2\log(2)}$.

CO(9-8) emission. The most extreme $OH^+$ emission line width in the QSO sample is associated with the obscured QSO MG J0414+0534.

Strong CO(9-8) emission is observed in all five quasars. The two obscured QSOs display significantly broader CO(9-8) line widths than the unobscured QSOs. The DSFGs span a wide range of CO(9-8) line widths (Riechers et al., 2021); however, the eight sources with blue–shifted $OH^+$ absorption all display wide (FWHM > 500 km $s^{-1}$) CO(9-8) line widths, similar to the obscured QSOs and wider than all the unobscured QSOs.

### 4.4.2 Derived Line Properties

From the fitted line properties we derive integrated $OH^+$ absorption optical depths,

$$\int \tau dv = -\ln\left(\frac{S_{trans}}{S_{cont}}\right)dv, \tag{4.1}$$

where $S_{trans}$ is the transmitted flux and $S_{cont}$ is the unobscured continuum flux level fitted at the central velocity of the line. We derive $OH^+$ emission and CO(9-8) line luminosities using the expressions given by Solomon et al. (1992).

We present these values in Table 4.3.

The integrated $OH^+$ absorption optical depths ($\int \tau_{OH^+,A}$) of the QSO sample lie at the low end of the DSFG sample (Fig.4.3a), roughly following the $\int \tau_{OH^+,A}$ vs dust temperature relation found by Riechers et al. (2021). The QSOs similarly follow the trend in increasing $OH^+$ emission line luminosity ($L'_{OH^+,E}$) with increasing $L_{FIR}$ set by the DSFGs (Riechers et al. 2021, Fig.4.3b). Interestingly, the scatter in this relation is greatly reduced when only considering the DSFGs with detections of blue–shifted $OH^+$ absorption (black points in Fig.4.3b).

Our sample of high–z QSOs follow the $L'_{CO(9-8)}$–$L_{FIR}$ correlation found in low–z galaxies (Liu et al., 2015), with MG J0414+0534 falling the farthest from the relation towards a lower $L'_{CO(9-8)}/L_{FIR}$ ratio (Fig.4.3c). Riechers et al. (2021) found that their sample of high-z DSFGs systematically deviates from this trend towards higher $L'_{CO(9-8)}/L_{FIR}$ ratios, however, this deviation is not seen in other high–z star-forming galaxies from the literature (see literature sample in Riechers et al. 2021).

## 4.5 Discussion

### 4.5.1 $OH^+$ Absorption

$OH^+(1_1\text{-}1_0)$ absorption has proven to be a reliable tracer of diffuse, predominantly atomic gas surrounding galaxies in turbulent halos (e.g., Indriolo et al., 2018). Recent observations have shown that it is also a reliable tracer of both inflowing (Berta et al., 2021; Riechers et al., 2021) and outflowing gas moving through the circum–galactic medium at high–$z$ (Indriolo et al., 2018; Butler et al., 2021; Riechers et al., 2021; Shao et al., 2022).

$OH^+$ absorption and emission are detected at similar rates ($\sim$ 75% and $\sim$ 65%, respectively) in the high–$z$ DSFGs and QSOs samples; however, Riechers et al. (2021) reported similar numbers of red– and blue–shifted $OH^+$ absorption in their DSFG sample, although the current number of high-$z$ sources showing clear evidence of infalling gas remain sparse (Berta et al., 2021;

Table 4.3: Derived QSO host galaxy properties and values from the Literature.

| Name | z | $T_d$ | $\mu L_{FIR}$[a] | $OH^+(1_1-1_0)$ Absorption | | $OH^+(1_1-1_0)$ Emission | | CO(9–8) Emission | |
|---|---|---|---|---|---|---|---|---|---|
| | | | | $\int \tau dv$ | N | $\mu L$ | $\mu L'$ | $\mu L$ | $\mu L'$ |
| | | [K] | $\log_{10}[L_\odot]$ | [km s$^{-1}$] | $10^{15}$[cm$^{-2}$] | $10^8[L_\odot]$ | $10^9$[K km s$^{-1}$ pc$^2$] | $10^8[L_\odot]$ | $10^9$[K km s$^{-1}$ pc$^2$] |
| MG J0414+0534 | 2.64[a] | 42.8 | $13.66^{+0.04}_{-0.03}$ | 77.4 ± 18 | 3.77 ± 0.87 | 6.37 ± 0.57 | 18.1 ± 1.6 | 6.09 ± 0.41 | 17.1 ± 1.2 |
| | | | | 70.6 ± 8.6 | 3.44 ± 0.42 | | | | |
| RX J0911+0551 | 2.79607[b] | 52.6 | $13.58^{+0.04}_{-0.03}$ | 24.3 ± 24 | 1.18 ± 0.27 | | | 6.73 ± 0.59 | 18.9 ± 1.7 |
| | | | | | | | 1.32 ± 0.45 | 6.00 ± 2.0 | |
| HE 1104-1805 | 2.3222[c] | 36.1 | $13.22^{+0.04}_{-0.04}$ | | | 1.94 ± 0.24 | 4.03 ± 0.51 | 1.44 ± 0.22 | 4.04 ± 0.61 |
| | | | | | | | 3.74 ± 0.26 | 10.5 ± 7.4 | |
| WFI J2026-4536 | 2.24265[c] | 50.3 | $13.81^{+0.02}_{-0.02}$ | 95.6 ± 22 | 4.66 ± 1.1 | | | 14.6 ± 0.35 | 41.0 ± 0.97 |
| PSS J2322+1944 | 4.12[a] | 47.4 | $13.58^{+0.01}_{-0.01}$ | 102 ± 55 | 4.99 ± 2.7 | 2.97 ± 0.68 | 8.44 ± 1.9 | 10.8 ± 0.28 | 30.2 ± 0.79 |

**Note:** a) FIR luminosities(40–120 $\mu$m ) from Stacey et al. (2018), not corrected for lensing magnification. b) Stacey et al. (2021), c) This work.



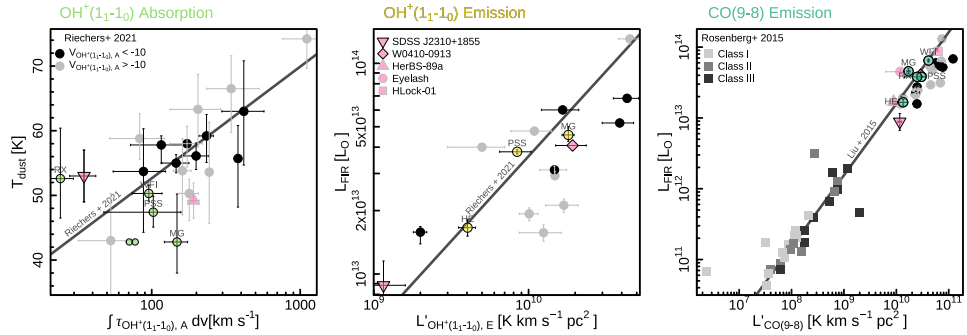


Figure 4.3: ***Left:*** *Integrated* $OH^+$ *optical depth vs dust temperature.* ***Middle:*** $OH^+$ *emission line luminosity vs* $L_{FIR}$ *(not corrected for magnification). The individual absorption components of MG J0414+0534 are indicated by smaller green points.* ***Right:*** *Magnification–uncorrected CO(9-8) emission line luminosity vs* $L_{FIR}$*. In this panel, we include the nearby star–forming galaxy sample studied by Rosenberg et al. (2015), categorised into classes of lowest (class I) to highest (class III) CO excitation. We compare our QSO sample with other high–z QSOs (W0410-0913 Stanley et al. 2021 and SDSS J2310+1955 Shao et al. 2022) and DSFGs (HerBS-89a Berta et al. 2021, the Eyelash Indriolo et al. 2018, HLock-01 Scott et al. 2011 and the sample from Riechers et al. 2021) from the literature. In all panels, we colour the sources from Riechers et al. (2021) with blue–shifted* $OH^+$ *absorption in black and colour the rest of the sample in grey.*



Riechers et al., 2021, and references therein). We do not find any occurrences of red–shifted absorption (Fig. 4.2), however, this may be biased by our selection of mostly Type 1 AGN systems (4/5 sources), as gas is more likely to fall into the host galaxy from perpendicular directions to the opening of the active nucleus where counter-acting radiation can efficiently escape from the host galaxy ([see, e.g., Shao et al., 2022). Alternatively, it could be a real difference between DSFGs and QSOs indicating that in QSO hosts, feeding from the CGM has stopped or been suppressed by feedback. The $OH^+$ absorption in the QSO sample does not otherwise display faster or broader lines (Fig. 4.2) and approximately follows the relation in optical depth with dust temperature set by the DSFGs (Fig. 4.3). This suggests that the ejection of gas traced by $OH^+$ absorption is not significantly affected by the presence of an active galactic nucleus, nor by whether the nucleus is obscured or not.

### 4.5.2 $OH^+$ Emission

In emission, $OH^+$ traces environments with high electron density (e.g., Gerin et al. 2016), which can arise in the dense hot gas in both photon and X-ray dense regions (PDRs, XDRs) and thus has been detected in both active (van der Werf et al., 2010; Stanley et al., 2021; Shao et al., 2022) and star–forming galaxies (Stanley et al. 2021; Riechers et al. 2021, Butler et al., in prep.).

The two obscured AGNs, MG J0414+0534 (see Fig. 4.1) and W0410−0913 (Stanley et al., 2021), display very broad ($> 1000$ km s$^{-1}$) $OH^+$ emission, with only one source in the DSFG sample of Riechers et al. (2021) with comparable linewidth. The unobscured QSOs lie in the same range as the rest of the DSFGs, possibly indicating that a contribution from XDRs is only significant during the obscured phase prior to the ejection of gas directly surrounding the AGN.

We do not see a boost in the $OH^+$ emission line luminosity w.r.t. the $L_{FIR}$ of any of the QSOs, finding instead good agreement with the DSFG relation. Considerable AGN contributions to the $L_{FIR}$ may, however, be expected in the obscured active systems (Schneider et al., 2015; Duras et al., 2017), which may overall maintain the $L'_{OH^+}/L_{FIR}$ ratio between the sources.

### 4.5.3 CO(9-8) Emission

CO(9-8) is predominantly excited by mechanisms associated with star formation, tracing the warm dense molecular gas in these regions. Active galactic nuclei can contribute to the CO(9-8) emission when present but typically do not dominate until higher J transitions (e.g., Li et al., 2020).

Whilst the QSO CO(9-8) line widths fall within the range covered by the DSFGs generally, we find that the obscured systems (MG J0414+0534 and W0410-0913 Stanley et al. 2021) show significantly broader CO(9-8) emission than the unobscured QSOs. This agrees with the result of Stacey et al. (2022) who showed that red, obscured QSOs (including MG J0414+0534) display broader ($\gtrsim$ 500 km $s^{-1}$) high-J CO lines than their unobscured counterparts. Comparing the high-J line widths with that of bulk gas tracers (i.e., a low-J CO line or [CI]), they show that the high-J lines in the reddened sources contained excess flux at higher velocities. They attribute this emission to molecular gas winds ejected by radiation pressure trapped by the obscuring material around the active nuclei. The narrow CO(9-8) lines observed in the unobscured QSOs thus indicate a phase after which the obscuring material has been ejected and the central AGN is no longer significantly impacting the kinematics of the molecular gas reservoir.



Blue–shifted $OH^+$ absorption is detected in QSO sources with both broad and narrow CO(9-8) emission but is only detected in DSFGs with broad CO(9-8). This may simply be caused by higher S/N in the QSO sample spectra and will require larger samples at high S/N to be confirmed. If so, this may indicate that neutral outflows in the halo require extreme galaxies (those displaying broad CO(9-8) emission or harbouring an AGN). If we follow the evolutionary picture where heavily star–forming galaxies evolve into quiescent galaxies via a short-lived QSO phase (Simpson et al., 2012), blue-shifted $OH^+$ absorption may be indicative of the energetic phase leading up to the obscured QSO phase and into an unobscured QSO phase (Petter et al., 2023). This scenario is consistent with the absence of red–shifted $OH^+$ absorption in the QSO sample. Larger samples targeting QSOs at all evolutionary stages are needed to test this hypothesis.

The deviation from the low–z $L'_{CO(9-8)} - L_{FIR}$ relation observed in the high–$z$ DSFGs was suggested to be driven by a higher prevalence of shock excitation in high–$z$ systems (Riechers et al., 2021). At low–$z$, sources categorised into Class I, II and III in order of increasing CO excitation, showed trends of falling above, on and both above and below the relation with greater scatter, respectively (Rosenberg et al. 2015, Fig.4.3). Riechers et al. (2021) noted that their sample of high-z DSFGs falls into a similar offset range as half the Class III sources are located below the relation. In addition, the highest $L'_{CO(9-8)}/L_{FIR}$ ratio was found in the binary active galactic nucleus NGC 6240, believed to be driven by shock excitation (Meijerink et al., 2013). Also citing $OH^+$ emission as an indicator of shocks, Riechers et al. (2021) suggest that shock heating drives the shift towards higher $L'_{CO(9-8)}/L_{FIR}$ ratios in their sample.

With the presence of both intense star formation and an active galactic nucleus, shocks may be expected to be even more prevalent in the high-$z$ QSO sample, particularly in the obscured and jetted MG J0414+0534. This source, however, displays the lowest $L'_{CO(9-8)}/L_{FIR}$ ratio in

our sample with the others, including W0410-0913 and other high–$z$ DSFGs from the literature, falling tightly on the low-$z$ relation. Furthermore, the presence of $OH^+$ emission indicates regions of high electron density (PDRs/XDRs) but not necessarily shocked gas. The QSOs, in any case, display the same behaviour in the $L'_{OH^+}-L_{FIR}$ plane, indicating that the deviation between samples in this plane is driven by mechanisms not associated with the $OH^+$ emission.

Contributions of the central AGN to the $L_{FIR}$ may be expected in the QSO hosts, accounting for the upwards vertical offset from the sample in Fig. 4.3. However, whilst considerable evidence for this is found in obscured QSOs (Duras et al., 2017; Schneider et al., 2015), studies of unobscured QSOs at high–$z$ do not find evidence for significant AGN contributions (Venemans et al., 2018, 2020; Butler et al., 2023). We again note that this deviation is not found between our sample and those high–$z$ DSFGs from the literature not included in Riechers et al. (2021). Thus we suggest that the deviation towards higher $L'_{CO(9-8)}/L_{FIR}$ ratios found for the sources studied in Riechers et al. (2021) may be a characteristic of that sample and not representative of high-$z$ DSFGs in general.

## 4.6 Conclusions

We have presented ALMA observations targeting the $OH^+$ ($1_1 - 1_0$) and CO(9-8) transitions in five $z \sim 2-4$ far-infrared luminous QSOs. The $OH^+$ ($1_1 - 1_0$) absorption and emission are seen at similar rates than in star–forming and active galaxies at high–$z$. $OH^+$ absorption is found only at systemic or blue–shifted velocities in the QSO sample, unlike in DSFGs where red–shifted absorption has also been detected (Berta et al., 2021; Riechers et al., 2021). We do not, however, find significant differences in the $OH^+$ absorption line properties between samples, suggesting that whilst that the central QSO plays a minor role in the ejection of the diffuse gas in the halo, the presence of a QSO may stop or suppress feeding from the CGM.

We find that obscured QSOs display broader $OH^+$ emission than unobscured and star–forming galaxies, likely driven by an increase in XDRs. We confirm the presence of broader ($FWHM_{CO(9-8)} > 500$ km s$^{-1}$) high-J CO emission in obscured QSOs than in unobscured QSOs, shown by Stacey et al. (2022) to indicate a QSO in the blow-out phase. Despite this difference, we do not see a difference in the outflows traced by $OH^+$. $OH^+$ outflows, however, are only detected in DSFGs with broad ($FWHM_{CO(9-8)} > 500$ km s$^{-1}$) CO(9-8) emission, possibly indicating that neutral outflows in the halo are associated with only the most extreme sources. Given the similarities seen in the blue-shifted $OH^+$ absorption line properties between QSO and dusty star–forming galaxies and the lack of red–shifted absorption in the QSO sample, we further suggest that blue-shifted absorption is indicative of the evolutionary phases shortly before the obscured QSO phase and moving into the unobscured QSO phase.



## Acknowledgements

This paper makes use of the following ALMA data: ADS/JAO.ALMA#2019.1.01802.S. ALMA is a partnership of ESO (representing its member states), NSF (USA) and NINS (Japan), together with NRC (Canada), MOST and ASIAA (Taiwan), and KASI (Republic of Korea), in cooperation with the Republic of Chile. The Joint ALMA Observatory is operated by ESO, AUI/NRAO and

NAOJ. This work benefited from the support of the project Z-GAL ANR-AAPG2019 of the French National Research Agency (ANR).

## 4.A ALMA Observation Details

Table 4.4: ALMA Observations

| Name | Ant.s | TOS [s] | Beam [″×″] | $\sigma_{100\mathrm{kms}^{-1}}$ [mJy beam$^{-1}$] |
|---|---|---|---|---|
| MG J0414+0534 | 46 | 3525 | $0.85 \times 0.96$ | 0.40 |
| RX J0911+0551 | 46 | 1131 | $0.98 \times 1.2$ | 0.29 |
| HE 1104-1805 | 44 | 2780 | $0.50 \times 0.65$ | 0.25 |
| WFI J2026-4536 | 44 | 1007 | $0.88 \times 1.0$ | 0.28 |
| PSS J2322+1944 | 48 | 3007 | $0.65 \times 0.90$ | 0.071 |



## 4.B Additional lines in WFI J2026-4536

We present the fitted and derived values of the spectral fits to the tentative detections of NH and $NH_2$ in WFI J2026-4536 in Table 4.5.

Table 4.5: Observed and derived line properties of NH and $NH_2$

| | | |
|---|---|---|
| NH($1_0 - 1_1$) Absorption | | |
| S | [mJy km s$^{-1}$] | $-1.78 \pm 86$ |
| v | [km s$^{-1}$] | $-572 \pm 1100$ |
| $\sigma$ | [km s$^{-1}$] | $145 \pm 560$ |
| $\int \tau \mathrm{dv}$ | [km s$^{-1}$] | $94.8 \pm 4590$ |
| NH($1_0 - 1_1$) Emission | | |
| S | [mJy km s$^{-1}$] | $0.890 \pm 0.15$ |
| v | [km s$^{-1}$] | $81.3 \pm 15$ |
| $\sigma$ | [km s$^{-1}$] | $86.5 \pm 15$ |
| $\mu$L | $10^7$[L$_\odot$] | $9.58 \pm 1.6$ |
| $\mu$L′ | $10^9$[L$_\odot$] | $2.97 \pm 0.49$ |
| $NH_2$($2_{2,0} - 2_{1,1}$) Emission | | |
| S | [mJy km s$^{-1}$] | $1.90 \pm 86$ |
| v | [km s$^{-1}$] | $204 \pm 4900$ |
| $\sigma$ | [km s$^{-1}$] | $169 \pm 1000$ |
| $\mu$L | $10^8$[L$_\odot$] | 2.05±93 |
| $\mu$L′ | $10^9$[L$_\odot$] | 6.35±288 |

# Bibliography

Berta, S., Young, A. J., Cox, P., et al. 2021, A&A, 646, A122, doi: 10.1051/0004-6361/202039743
Butler, K. M., van der Werf, P. P., Topkaras, T., et al. 2023, ApJ, 944, 134, doi: 10.3847/1538-4357/acad03
Butler, K. M., van der Werf, P. P., Rybak, M., et al. 2021, ApJ, 919, 5, doi: 10.3847/1538-4357/ac0c7a
Duras, F., Bongiorno, A., Piconcelli, E., et al. 2017, A&A, 604, A67, doi: 10.1051/0004-6361/201731052
Falgarone, E., Zwaan, M. A., Godard, B., et al. 2017, Nature, 548, 430, doi: 10.1038/nature23298
Fan, L., Knudsen, K. K., Fogasy, J., & Drouart, G. 2018, ApJ, 856, L5, doi: 10.3847/2041-8213/aab496
Feruglio, C., Maiolino, R., Piconcelli, E., et al. 2010, A&A, 518, L155, doi: 10.1051/0004-6361/201015164
Fluetsch, A., Maiolino, R., Carniani, S., et al. 2021, MNRAS, 505, 5753, doi: 10.1093/mnras/stab1666
Gerin, M., Neufeld, D. A., & Goicoechea, J. R. 2016, ARA&A, 54, 181, doi: 10.1146/annurev-astro-081915-023409
Ginolfi, M., Jones, G. C., Béthermin, M., et al. 2020, A&A, 633, A90, doi: 10.1051/0004-6361/201936872
Governato, F., Brook, C., Mayer, L., et al. 2010, Nature, 463, 203, doi: 10.1038/nature08640
Inada, N., Oguri, M., Shin, M.-S., et al. 2012, AJ, 143, 119, doi: 10.1088/0004-6256/143/5/119
Indriolo, N., Bergin, E. A., Falgarone, E., et al. 2018, ApJ, 865, 127, doi: 10.3847/1538-4357/aad7b3
Jones, G. C., Maiolino, R., Caselli, P., & Carniani, S. 2019, A&A, 632, L7, doi: 10.1051/0004-6361/20193698910.48550/arXiv.1911.09967
Kochanek, C. S., Falco, E. E., Impey, C. D., et al. 1999, in American Institute of Physics Conference Series, Vol. 470, After the Dark Ages: When Galaxies were Young (the Universe at 2 Z 5), ed. S. Holt & E. Smith, 163–175, doi: 10.1063/1.58598
Li, J., Wang, R., Riechers, D., et al. 2020, ApJ, 889, 162, doi: 10.3847/1538-4357/ab65fa
Liu, D., Gao, Y., Isaak, K., et al. 2015, ApJ, 810, L14, doi: 10.1088/2041-8205/810/2/L14
Madau, P., & Dickinson, M. 2014, ARA&A, 52, 415, doi: 10.1146/annurev-astro-081811-125615
McMullin, J. P., Waters, B., Schiebel, D., Young, W., & Golap, K. 2007, in Astronomical Society of the Pacific Conference Series, Vol. 376, Astronomical Data Analysis Software and Systems XVI, ed. R. A. Shaw, F. Hill, & D. J. Bell, 127
Meijerink, R., Kristensen, L. E., Weiß, A., et al. 2013, ApJ, 762, L16, doi: 10.1088/2041-8205/762/2/L16
Petter, G. C., Hickox, R. C., Alexander, D. M., et al. 2023, arXiv e-prints, arXiv:2302.00690, doi: 10.48550/arXiv.2302.00690
Planck Collaboration, Ade, P. A. R., Aghanim, N., et al. 2016, A&A, 594, A13, doi: 10.1051/0004-6361/201525830
Riechers, D. A., Cooray, A., Pérez-Fournon, I., & Neri, R. 2021, ApJ, 913, 141, doi: 10.3847/1538-4357/abf6d7
Rosenberg, M. J. F., van der Werf, P. P., Aalto, S., et al. 2015, ApJ, 801, 72, doi: 10.1088/0004-637X/801/2/72
Schneider, R., Bianchi, S., Valiante, R., Risaliti, G., & Salvadori, S. 2015, A&A, 579, A60, doi: 10.1051/0004-6361/201526105
Scott, K. S., Lupu, R. E., Aguirre, J. E., et al. 2011, ApJ, 733, 29, doi: 10.1088/0004-637X/733/1/29
Shao, Y., Wang, R., Carilli, C. L., et al. 2019, ApJ, 876, 99, doi: 10.3847/1538-4357/ab133d
Shao, Y., Wang, R., Weiss, A., et al. 2022, A&A, 668, A121, doi: 10.1051/0004-6361/202244610
Simpson, J. M., Smail, I., Swinbank, A. M., et al. 2012, MNRAS, 426, 3201, doi: 10.1111/j.1365-2966.2012.21941.x

Solomon, P. M., Downes, D., & Radford, S. J. E. 1992, ApJ, 398, L29, doi: 10.1086/186569
Spilker, J. S., Aravena, M., Béthermin, M., et al. 2018, Science, 361, 1016, doi: 10.1126/science.aap8900
Spilker, J. S., Aravena, M., Phadke, K. A., et al. 2020, ApJ, 905, 86, doi: 10.3847/1538-4357/abc4e6
Stacey, H. R., Costa, T., McKean, J. P., et al. 2022, MNRAS, 517, 3377, doi: 10.1093/mnras/stac2765
Stacey, H. R., McKean, J. P., Robertson, N. C., et al. 2018, MNRAS, 476, 5075, doi: 10.1093/mnras/sty458
Stacey, H. R., McKean, J. P., Powell, D. M., et al. 2021, MNRAS, 500, 3667, doi: 10.1093/mnras/staa3433
Stanley, F., Knudsen, K. K., Aalto, S., et al. 2021, A&A, 646, A178, doi: 10.1051/0004-6361/202037888
Travascio, A., Zappacosta, L., Cantalupo, S., et al. 2020, A&A, 635, A157, doi: 10.1051/0004-6361/201936197
van der Werf, P. P., Isaak, K. G., Meijerink, R., et al. 2010, A&A, 518, L42, doi: 10.1051/0004-6361/201014682
Venemans, B. P., Decarli, R., Walter, F., et al. 2018, ApJ, 866, 159, doi: 10.3847/1538-4357/aadf35
Venemans, B. P., Walter, F., Neeleman, M., et al. 2020, ApJ, 904, 130, doi: 10.3847/1538-4357/abc563